PCCP



PAPER



Cite this: Phys. Chem. Chem. Phys.. 2024, 26, 4614

Lifetimes and decay mechanisms of isotopically substituted ozone above the dissociation threshold: matching quantum and classical dynamics†

Viatcheslav Kokoouline, **D*** Alexander Alijah **D** and Vladimir Tyuterev **D*** cd

Energies and lifetimes of vibrational resonances were computed for 18 O-enriched isotopologue 50 O $_{\pi}$ = ${}^{16}O^{16}O^{18}O$ and ${}^{16}O^{18}O^{16}O$ } of the ozone molecule using hyperspherical coordinates and the method of complex absorbing potential. Various types of scattering resonances were identified, including roaming OO-O rotational states, the series corresponding to continuation of bound vibrational resonances of highly excited bending or symmetric stretching vibrational modes. Such a series become metastable above the dissociation limit. The coupling between the vibrationally excited O2 fragment and rotational roaming gives rise to Feshbach type resonances in ozone. Different paths for the formation and decay of symmetric ¹⁶O¹⁸O¹⁶O and asymmetric species ¹⁶O¹⁶O¹⁸O were also identified. The symmetry properties of the total royibronic wave functions of the ¹⁸O-enriched isotopologues are discussed in the context of allowed dissociation channels.

Received 5th September 2023, Accepted 13th December 2023

DOI: 10.1039/d3cp04286c

rsc.li/pccp

I. Introduction

The study of isotopic variations has a wide range of applications from nuclear astrophysics to geochemistry and biochemistry. As an example, such studies can provide an insight into the climate in the past, measuring isotope composition of compounds preserved in ancient terrestrial materials, ice and sediment cores. 1-6 Oxygen is one of the most abundant elements on the Earth that has three stable isotopes: ¹⁶O, ¹⁷O and ¹⁸O. The origin and abundance of these isotopes could provide information on nuclear processes in nova and supernova stars:⁷⁻¹² ejected traces of stars were found in unusual isotopic abundance in several-billion-year-old meteorites. 6,13 Different isotopes can react at different rates. Usually, isotope effects scale proportionally to relative mass differences, and the corresponding mass fractionation laws for the same process but involving different isotopologues are called mass-dependent¹⁴ fractionation (MDF). The isotopic variability of oxygen in the solar system, along with large

In some cases, the isotopic reaction products show significant difference from the usual MDF laws, and they are called mass-independent fractionations (MIFs) or, sometimes, non-MDF effects. For details, see ref. 4, 6, and 18–21 and references therein. This MIF effect is the most pronounced effect for the isotopic variant of the ozone molecule.²²⁻³² It has been observed in meteorites, 13 in laboratory electric discharge experiments, 23,24 and in the upper atmosphere. 22,25-27,33 This has puzzled the chemistry community for nearly four decades, which is considered as a "fascinating and surprising aspect...of selective enrichment of heavy ozone isotopomers"34 and "a wellrecognized milestone in the study of isotope effect".31

The MIF discovery was a motivation for a large number of experimental and theoretical studies. Experiments reported by the Mauersberger group^{26,27,35,36} and by Janssen and coworkers^{29,37,38} have provided recombination rate coefficients

mass dependent fractionation on the Earth, with a difference between the atmosphere and hydrosphere was the subject of many measurements as recently reviewed by Ireland et al. 12 A higher fraction of the heavy ¹⁸O isotope was reported in the lower atmosphere compared to the ocean water. ¹⁵ An isotopic enrichment in oxygen is consistent with the MDF and is attributed to the biological activity. 15,16 Oxygen isotopes in single-celled organism sediments provide information on changes in ocean temperatures over the last 70 million years. 17 Recent astrophysical studies suggest that the distribution of oxygen isotopes can help understand the formation processes of the solar system and other exoplanetary systems. 12

^a Department of Physics, University of Central Florida, Orlando, FL 32816, USA. E-mail: Vyacheslav.Kokoulin@ucf.edu

^b Groupe de Spectrometrie Moléculaire et Atmospherique, UMR CNRS 7331, University of Reims Champagne-Ardenne, Reims Cedex 2, F-51687, France

^c Laboratory of Molecular Quantum Mechanics and Radiative transfer, Tomsk State University, Tomsk, Russia

^d Laboratory of Theoretical Spectroscopy, V.E. Zuev Institute of Atmospheric Optics, Russian Academy of Sciences, Tomsk, 634055, Russia

[†] Electronic supplementary information (ESI) available. See DOI: 10.1039/ d3cp04286c

for various types of isotopic combinations. It is most often assumed^{6,30} that isotopic anomalies occur at the first step of formation of the metastable complex in the Lindemann energy transfer mechanism,

$$^{n}O^{m}O + ^{k}O \rightleftharpoons ^{N}O_{3}^{*},$$
 (1)

followed by stabilisation collision

$${}^{N}\mathrm{O}_{3}^{*} + \mathrm{M} \rightarrow {}^{N}\mathrm{O}_{3} + \mathrm{M} \tag{2}$$

with third body M, which takes off an excess of energy to allow the complex falling down to one of the ozone potential wells. The third body could be N2 or O2 under atmospheric conditions, or Ar in many experimental laboratory studies. Here, the left-upper case indices n, m, and k refer to atomic masses of 16, 17, or 18 of oxygen isotopes (different or the same) and N = n + 1m + k is the atomic mass of the ozone isotopologue. The asterisk means that the collision of eqn (1) produces an excited metastable vibrational complex above the dissociation energy of the ozone potential energy surface (PES). The stabilization step of eqn (2) depends on lifetimes of the metastable complexes (scattering resonances) that should be sufficiently long for the complex to encounter a third body before it dissociates back to atomic and diatomic fragments. There are three possible outcomes for ^NO₂* after the formation step: ³⁰ either it dissociates to the same products at the left of eqn (1) or to another isotopomer (isotope exchange reaction), or it can be stabilized (stabilization step). At certain pressure and temperature, other reactions like the radical-complex mechanism may also play an important role^{39,40} in ozone formation.

Janssen et al.41 have found that the reaction rates for the different isotopic compositions correlate with the difference in the zero-point energies (ZPE) of various diatomic partners in eqn (1). Marcus and co-workers^{31,42-44} have developed first theoretical models for the MIF using the RRKM theory based on certain statistical assumptions. They have shown the importance of difference Δ_{ZPE} in ZPEs of isotopologues⁴⁵ in the recombination of ozone and its isotope dependence, which was confirmed by later studies reviewed in ref. 30 and is now considered as well-understood.31 In contrast, the mechanism of the experimentally determined difference in the rates of formation of symmetric (such as ¹⁶O¹⁸O¹⁶O) versus asymmetric (such as 16O16O18O) ozone isotopologues was difficult to explain based on this model. To this end, Marcus and coworkers have empirically introduced the symmetry driving η -effect. ^{31,42,43} The η -effect is a non-statistical effect, requiring detailed quantum calculations and making major difficulties for further theoretical interpretations.

Earlier works and related issues have been reviewed by Schinke et al., 30 and Marcus. 31 Following the suggestion by Heidenreich and Thiemens,²⁴ it was assumed that the observed MIF effect could be linked to the lifetimes of the metastable complexes, 30,46,47 though this idea remained controversial. 48 Since then, many theoretical studies have reported significant improvements of ab initio PESs,34,49-52 dipole moment surface53 and energy level calculations, 50,54-57 along with experimental

results on laser spectroscopy measurements made for ozone isotopologues near the dissociation threshold.⁵⁸⁻⁶¹

The isotopic anomalies in simpler two-body oxygen isotopic exchange reactions, which can be considered as competing with the energy transfer mechanism at the stabilisation step of O₃*, have been intensively studied both experimentally^{29,62-64} and theoretically. 30,65-71 Both the experiment and the theory revealed nonstatistical behaviour of the reaction.^{72,73}

Isotopic branching ratios of electronic and isotopic photodissociation channels of ozone using quantum mechanical wave packet propagation were considered in ref. 74 and 75. The dynamics in OO + O + Ar complexes was investigated to compare the temperature dependence of ozone formation⁴⁰ with experimental data, whereas isotopic substitutions in the O₃-Ar system were studied in ref. 76. The question whether the topological Berry phase⁷⁷ near the conical intersection in the O₃ PES should be included in the calculation of rovibronic states of the ozone molecule in its electronic ground state has been considered in ref. 78.

Many efforts have been devoted to further theoretical modelling of the MIF processes: various possible mechanisms: classical trajectory and quantum mechanical calculations have been carried out by groups of Schinke^{30,46,64,79,80} and Babikov et al. 48,81-85 Other approaches have been reported in ref. 47 and 86-90, and some of them not necessarily based on the stabilisation of O₃* have been discussed in ref. 47, but a full understanding of this "strange and unconventional" MIF effect is still lacking. This particularly concerns the symmetry driving effects, for which additional research is needed.⁸²

It is now well established 4-6 that the ozone MIF is not a minor and exotic phenomenon of a limited impact: its effect is photochemically transferred to many oxygen-bearing species including atmospheric CO2, O2, and water in the early solar system. 6,91,92 There is a wide area of interdisciplinary scientific fields, including atmospheric physics, geo- and cosmochemistry or climate research, ^{5,93-97} where the ozone isotope composition, or molecular effects of isotope fractionation, plays a major role.^{98–100}

The state-of-the art of the MIF studies and possible impacts across various branches of science have been described in recent exhaustive reviews by Thiemens and Lin,5 Thiemens et al.,20 Dauphas and Schauble,4 and Carlstad and Boering,6 who have concluded that "The origin in chemical physics of the large, robustly measured mass-independent enrichments in ozone resulting from the three-body ozone formation reaction remains elusive and represents an intriguing chemical physics puzzle that deserves further study".

In this work, we report a comparative investigation of lifetimes of the vibrational metastable ⁵⁰O₃* ozone complex having different partial decay rates into different allowed decay channels. The ⁵⁰O₃* complex is composed by isotopic substitution in the main ⁴⁸O₃* ozone with one heavy ¹⁸O oxygen atom. In a simplified way, it could be viewed as being inherited from symmetric (16O18O16O)* and asymmetric (16O16O18O)* species, though the true picture implies some mixed variants as well. The motivation is to obtain more detailed insight into possible

isotopic outcomes of reaction (1) at the first step of ozone formation. The calculations are based on the spectroscopically accurate *ab initio* PES⁵⁰ used to obtain the metastable states above the dissociation threshold D_0 , which currently agrees the best with the observed data for the bound state levels of the ozone isotopologues^{57,60,101,102} up to about 95% of D_0 .

This study is structured as follows. In the next section, the potential of ozone is discussed from a point of view of vibrational scattering states of O₃ and the method of hyperspherical coordinates with the complex absorbing potential, adapted to the theoretical description of ozone vibrational resonances. Section III is devoted to the symmetry of rovibrational resonances of ozone isotopologues. In Section IV, the results of energies, lifetimes and other observables related to the obtained vibrational resonances are presented, while in Section V, different types of resonances and different decay mechanisms are discussed. Section VI concludes the article.

II. Nuclear dynamics in hyperspherical coordinates

In its ground electronic state, ozone has an isosceles triangular equilibrium configuration, *i.e.*, the C_{2v} point group in the case of three equal oxygen isotopes. There are equivalent configurations obtained from each other by permutations of the three nuclei. Tannor¹⁰³ has demonstrated that the lowest ground state ${}^{1}A_{1}$ in the C_{2v} group can be viewed as one of the two components of the ${}^{1}E'$ electronic state of the D_{3h} group that is degenerate at the equilateral configuration and split in the ¹A₁ and ${}^{1}B_{2}$ states in the C_{2v} group by Jahn-Teller coupling. The Jahn-Teller coupling produces three equivalent wells with three minima at the isosceles geometries. The three potential wells are separated by a large barrier, so that the lowest vibrational levels can be considered neglecting permutations of identical nuclei. However, at energies approaching the dissociation energy and above, the particle permutation should be accounted for and an accurate description of the vibrational dynamics should include the motion in the three potential wells at the same time.

Hyperspherical coordinates, in particular, the so-called democratic hyperspherical coordinates, 104-109 are well suited for the description of the nuclear dynamics of the highly excited ozone molecule, as all nuclear configurations are treated on equal footing and hence, the full permutational symmetry can be exploited. They are obtained by symmetrization of the three equivalent Jacobi systems. The hyperspherical coordinates provide a mapping of the nuclear configurations on a hemisphere with hyper-radius ρ , which determines the size of the threeparticle system. On this hypersphere, two angles describe the shape of the triangle formed by the three particles: θ , with $0 \le \theta$ $\theta \leq \pi$ is the polar angle, and ϕ , with $0 \leq \phi \leq 2\pi$ is the azimuthal angle. Pairs of configurations with θ and π - θ are identical, i.e. they correspond to the same distances between the three particles. Fig. 1 shows how the different geometrical forms of the triangles are mapped on the upper half of the hypersphere with $0 \le \theta \le \pi/2$.

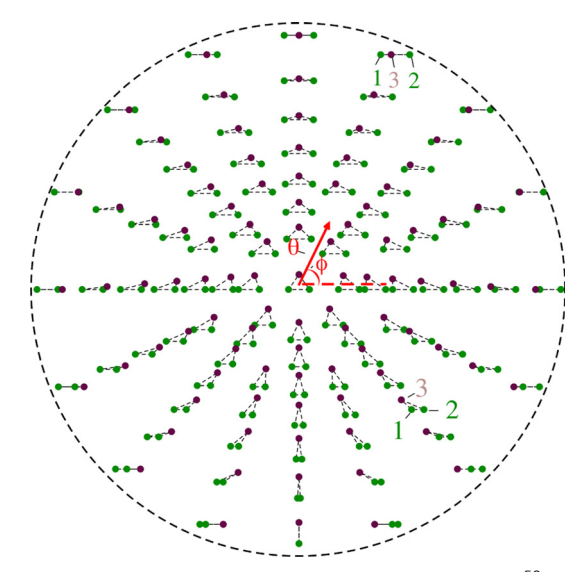


Fig. 1 Definition of hyperangles θ and ϕ . In the case of the $^{50}\text{O}_3$ ozone isotopologue, the light oxygen atoms ^{16}O are shown in green color, whereas the heavy oxygen ^{18}O is shown in brown color. The origin of the hyperspherical angle ϕ is at 03:00 h, and the angle advances counterclockwise.

The geometry of the ozone PES is illustrated in Fig. 2. On the left panel of the figure, the value of the hyper-radius $\rho=4a_0$ is near the minima (three equilibrium geometries) of the PES. As the hyper-radius increases beyond the value of equilibrium, the potential wells gradually disappear (middle and right panels in Fig. 2), and the three conventional configurations are no longer isolated. Instead, three valleys emerge that connect them (middle and right panels in Fig. 2). They represent a dioxygen molecule and a distant oxygen atom. Motion in the valley between the two colinear equatorial $\theta=\pi$ positions then describes the motion of the distant oxygen atom from one side to the other side of the diatomic molecule. This motion can be understood with the help of Fig. 1. Let us begin this

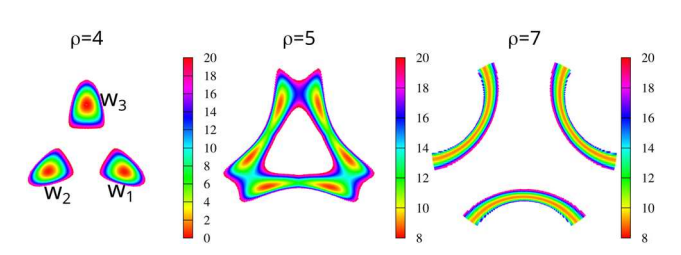


Fig. 2 The maps of the *ab initio* potential energy surface in units of $1000~{\rm cm}^{-1}$ of the ozone molecule in the three-wells represented in a polar coordinate system for three values of the hyper-radius ρ . Possible geometrical arrangements $866 = {}^{18}{\rm O}^{16}{\rm O}^{16}{\rm O}$, $668 = {}^{16}{\rm O}^{18}{\rm O}$, and $686 = {}^{16}{\rm O}^{18}{\rm O}^{16}{\rm O}$ of the oxygen nuclei in the potential wells ${\rm w_1}$, ${\rm w_2}$, and ${\rm w_3}$ correspond to conventional $C_{\rm s}$ and $C_{\rm 2v}$ point group configurations. The left panel shows the PES cut for the near-equilibrium value of the hyperradius $\rho = 4$ bohrs where the wells are isolated. The middle and right panels show the PES for larger values of the hyper-radius exhibiting three potential valleys for the angular (roaming) motion of the detached atom around the diatomic fragment. Another visual representation of OO–O roaming is given by Jacobi coordinates (r_{66} , R_{8} , γ_{8}) or (r_{68} , R_{6} , γ_{6}) shown in Fig. 3.

analysis at the equator $\theta = \pi/2$ and $\phi = \pi/2$ or at 00:00 hours (if we use clock time notations looking at the hemisphere from above), which corresponds to the symmetric linear 132 structure, and then moves clockwise. The brown atom 3 18O, then approaches atom 1, the left of the two is shown ¹⁶O in green color, and until at about 02:30 hours, 3 and 1 sit upon each other. Continuing clockwise, atom 3 then overpasses atom 1, and we have configuration 312. Passage between the linear structures at 01:00 and 04:00, while θ is changing from $\pi/2$ to somewhat smaller values and then back to $\pi/2$ (departing from the equator), approximately corresponds to a roaming motion of atom 2 around the diatomic 13, which can also be viewed as rotation of the diatomic 13 in the reference frame of the three atoms. Such a motion, departing from the equator, bypasses the singularity. Continuing clockwise, atom 1 approaches 2 until at 06:00 where they are at the same position, giving rise to another singularity of the potential. Motion around this singularity describes the roaming brown atom 3 (18O). Continuing clockwise from 06:00, we find configurations 123, and 2 approaches 3, until at about 10:00 we arrive at the third singularity, where the positions of 2 and 3 coincide. Motion around this singularity describes roaming atom 1. We finally note that all C_{2v} configurations are on the line connecting 00:00 with 06:00. The minimum of the ¹⁶O¹⁸O¹⁶O isotopologue at the bottom of the PES is marked as w₃ shown in Fig. 2. Such a roaming motion may also be visualised in Jacobi coordinates, as shown in Fig. 3, which are the natural coordinates to describe dissociating O₂ + O. A similar roaming rovibrational dynamics was previously observed in other systems, such as in $\rm H_2CO^{110,111}$ and $\rm CH_3NO_2^{\ 112}$ and, more recently, also discussed in ref. 113 in relation to ozone.

To obtain wave functions, energies, and lifetimes of vibrational bound states and resonances, the approach described in ref. 54 and 105-107 was employed. Here, we give only a very brief description. The Schrödinger equation

$$[T(\rho, \theta, \phi) + V(\rho, \theta, \phi)]\Phi_{\mathbf{v}}(\rho, \theta, \phi) = E_{\mathbf{v}}\Phi_{\mathbf{v}}(\rho, \theta, \phi). \tag{3}$$

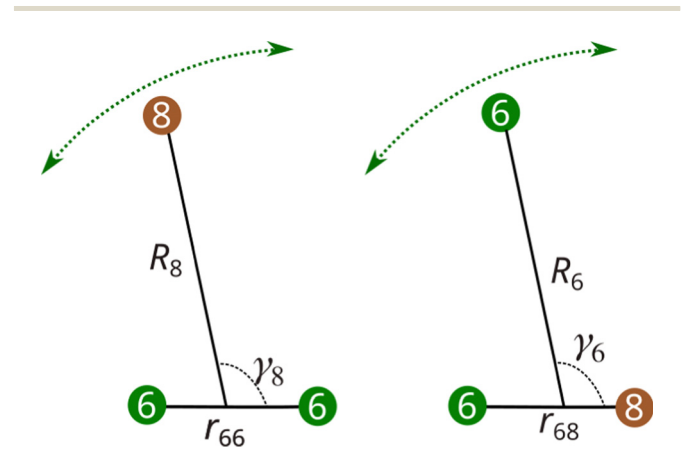


Fig. 3 Jacobi coordinates for possible roaming motion of one oxygen atom around the diatomic fragment in the vibrationally excited ozone isotopologue ⁵⁰O₃ with one ¹⁸O substitution. Standard abbreviated notations for the light 6 \leftrightarrow ¹⁶O and heavy 8 \leftrightarrow ¹⁸O oxygen atoms are used.

is solved in hyperspherical coordinates in a two-step procedure. First, we solve for a number of fixed values of the hyperradius, $\rho_i(j=1, 2, ..., N_\rho)$, and the two-dimensional angular equation

$$\left[\hbar^2 \frac{\Lambda^2 + \frac{15}{4}}{2\mu\rho_j^2} + V(\rho_i; \theta, \phi)\right] \varphi_a(\rho_j; \theta, \phi) = U_a(\rho_i) \varphi_a(\rho_j; \theta, \phi),$$
(4)

where Λ^2 is the grand angular momentum squared ^{104,114} and μ is the three-particle reduced mass. The solution of eqn (4) produces adiabatic curves $U_a(\rho)$ and eigenfunctions $\varphi_a(\rho; \theta, \phi)$, defining a set of hyperspherical adiabatic (HSA) channels numerated with index a. Angular boundary conditions are employed to obtain solutions with a well-defined permutational symmetry according to Section III. The lowest 240 of these curves are shown in Fig. 4. Asymptotically, different adiabatic curves correspond to various rovibrational channels of the oxygen molecules 16O2 or 16O18O produced when O3 dissociates. Each channel is characterized (labeled) with a label of the type of the dimer in the channel (16O2 or 16O18O), and the rotational angular momentum $j_{\rm d}$ of the dimer, and the vibrational quantum number v_d .

The wave function Φ_{v} in eqn (3) is then developed as

$$\Phi_{\rm v}(\rho,\theta,\phi) = \sum_{a} \psi_{a}(\rho_{j}) \varphi_{a}(\rho_{j};\theta,\phi), \tag{5}$$

where $\psi_a(\rho_i)$ are ρ -dependent coefficients, which in turn are expanded in a discrete variable representation (DVR) basis $\pi_i(\rho)$, following ref. 115,

$$\psi_a(\rho) = \sum_j c_{j,a} \pi_j(\rho). \tag{6}$$

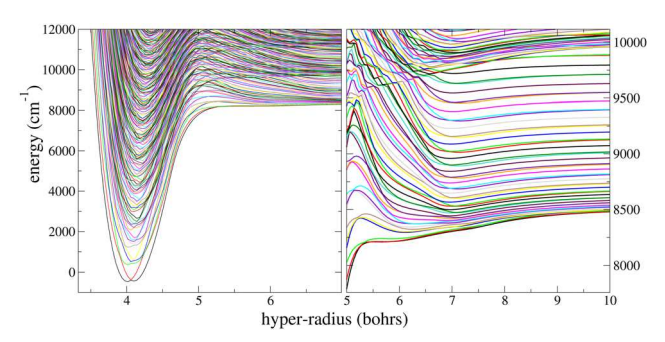


Fig. 4 Hyperspherical adiabatic curves $U_a(\rho)$ at J=0 as a function of hyper-radius obtained for the ⁵⁰O₃ ozone isotopologue in the first step of variational calculations eqn (4). In this figure, the energy origin is chosen at the ground vibrational level $^{16}O^{18}O^{16}O$ situated 1416.602 cm $^{-1}$ above the PES minimum. The left panel shows the global view for the adiabatic curves of the A₁ irreducible representation of the permutation-inversion symmetry group $C_{2v}(M)$. The right panel is zoomed on the region near the lowest dissociation thresholds and the asymptotic behavior at large ho

Inserting the two above expansions into the initial Schrödinger equation (3), one obtains

$$\sum_{j',a'} \left[\left\langle \pi_{j'} \right| - \frac{\hbar^2}{2\mu} \frac{\mathrm{d}^2}{\mathrm{d}\rho^2} |\pi_j \right\rangle \mathcal{O}_{j'a',ja} + U_a(\rho_j) \delta_{j',j} \delta_{a'a} \right] c_{j'a'} = E \sum_{a'} \mathcal{O}_{ja',ja} c_{ja'}$$

$$\tag{7}$$

with

$$\mathcal{O}_{j'd',ja} = \left\langle \varphi_{d'}(\rho_{j'};\theta,\phi) \mid \varphi_{a}(\rho_{j};\theta,\phi) \right\rangle. \tag{8}$$

The matrix elements of the second-order derivative with respect to ρ in the above equation are calculated analytically (see, for example, ^{116,117} and references therein). To obtain the continuum solutions, a complex absorbing potential was added at large ρ -values. ¹⁰⁶

The convergence tests for the obtained energies and lifetimes were performed. The parameters, to which the energies and lifetimes are sensitive the most, are the numbers $(N_{\theta}, N_{\phi}, N_{\rho})$ of basis functions in hyperspherical coordinates, the number $N_{\rm a}$ of adiabatic states in the expansion of eqn (5), and the position $\rho_{\rm c}$, the strength $V_{\rm c}$, and the length $L_{\rm c}$ of the complex absorbing potential. Having performed the convergence tests, we found that the values $N_{\theta}=120$, $N_{\phi}=300$, $N_{\rho}=200$, $N_{\rm a}=180$, $\rho_{\rm c}=9$ bohrs, $V_{\rm c}=0.005$ Hartree, and $L_{\rm c}=6$ bohrs provide convergence for energies of the resonances with the uncertainty of about 0.2 cm⁻¹, and for the relative uncertainty of lifetimes of about 0.2%. The uncertainty in energies of calculated bound states is much better than 0.2 cm⁻¹, and it is of the order of 10^{-4} cm⁻¹.

Looking at wave functions of vibrational states gives an intuition about motion in hyperspherical coordinates. An example of such wave functions is shown in Fig. 5, where the hyper-angular dependence at a fixed value of $\rho=9$ bohrs of a state with energy $E=8542.82~{\rm cm}^{-1}$ is demonstrated. The green circles refer to the ¹⁶O isotopes and the brown circles refer to the heavy ¹⁸O isotope. At the right PES valley, the Jacobi angle γ_6 of the rotation of ¹⁶O around the ¹⁸O¹⁶O diatomic fragment varies from 0 to π , whereas the average value of the hyperangle is $\langle \phi \rangle = 30^{\circ}$.

Symbols w_1 , w_2 and w_3 shown in Fig. 5 mark minima of the three potential wells (situated at a smaller hyper-radius, $\rho \sim$ 4.2 bohrs). At this relatively large value of the hyper-radius ρ = 9 bohrs (see also Fig. 4), one of the three atoms is almost uncoupled from the diatomic molecule. Classical roaming motion of an atom around the O2 dimer is clearly represented by nodal structures (red and blue areas in the figure) in three sectors of the complete hyperangular space (the PES valleys). The fact that the wave function is not negligible in all three sections means that the motion is delocalised in the three channels, corresponding to the three asymptotic arrangements: ¹⁶O-¹⁶O¹⁸O and ¹⁸O-¹⁶O₂, with the first one being doublydegenerate. The wave function in the left PES valley, near 9:00-11:00, is the same as in the right one, 1:00-3:00, because the two valleys are obtained from each other by a permutation of the identical atoms ¹⁶O. The valley at the bottom, near 5:00-7:00, corresponds to the ¹⁸O atom separated from ¹⁶O₂. The wave function in this region is not the same as in the two other

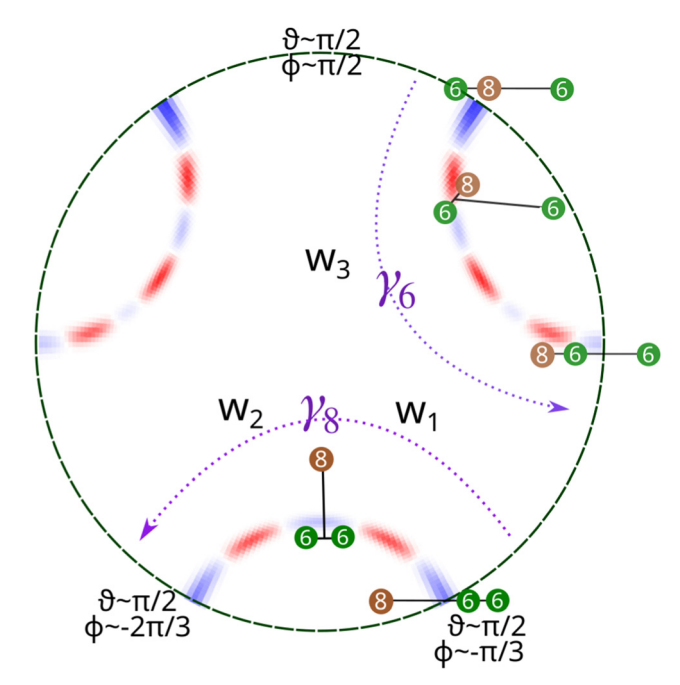


Fig. 5 The figure shows the hyper-angular dependence of the wave function of the state with energy E=8542.82 at $\rho=9$ bohrs. Symbols w_1, w_2 and w_3 mark equilibrium locations of the potential wells. Classical roaming $^{16}O^{16}O^{-18}O$ corresponds to nodal lines (red and blue areas) of the wave function. The green circles mark positions of the light ^{16}O isotopes and the brown circles of the heavy ^{18}O isotope. The Jacobi angle γ_8 of the rotation ^{18}O of around the $^{16}O^{16}O$ diatomic fragment varies from 0 to π .

valleys. Nodes of the wave function in the three valleys are aligned mainly along the ϕ coordinate and not perpendicular to it. This indicates that the diatomic O_2 is in its vibrational ground state.

In contrast to the wave function of Fig. 5 with the ground vibrational level of O_2 in all three dissociation channels, Fig. 6 gives an example of the state with the wave function having in the two $^{16}O + ^{16}O^{18}O$ valleys (9:00–11:00 and 1:00–3:00) a node perpendicular to ϕ and mainly along the θ coordinate. A node along θ corresponds to the vibrating (ν = 1) O_2 molecules. One can also see in the lower valley (5:00–7:00) that the motion is just characterized by roaming, *i.e.* the relative rotation of ^{18}O and $^{16}O_2$. This state is a resonance state with energy 9955 cm $^{-1}$, which decays partially to the $^{16}O + ^{16}O^{18}O$ (ν = 1, j = 0) channel and partially to $^{18}O + ^{16}O_2$ (ν = 0, j = 16). Amplitudes in other symmetry-allowed channels are significantly smaller.

The wave function of that state is also shown in Fig. 7 in a different form: by surfaces of a constant amplitude (positive – red color, negative – blue color) in all three hyperspherical dimensions ρ , θ , ϕ . The three hyperspherical coordinates are arranged in the same way as in a familiar arrangement of standard spherical coordinates, *i.e.* ρ corresponds to the distance from the center of the coordinate system, the angles θ and ϕ represent polar and azimuthal angles of orientation in a Cartesian coordinate system with axes x, y, and z. Therefore, the dissociation region in this picture corresponds to large distances from the origin, and the minima of the potential $w_{1,2,3}$

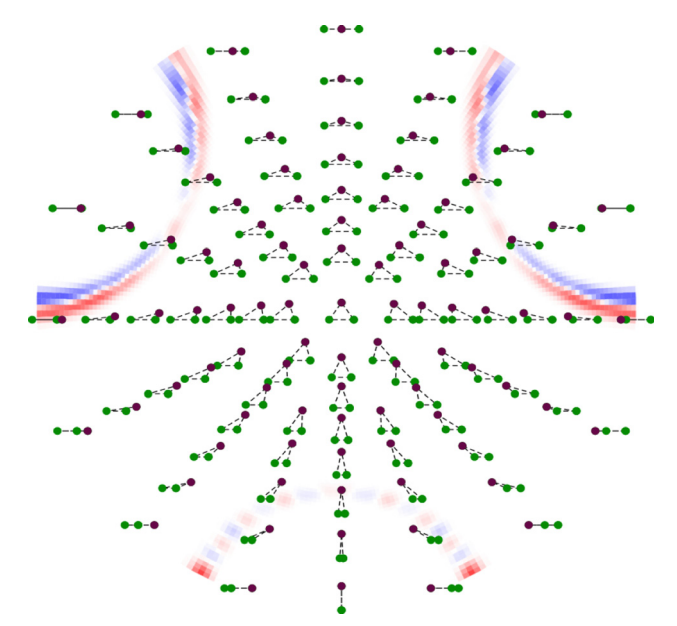


Fig. 6 Wave function (red and blue areas) of a resonant state with energy 9955 cm⁻¹ shown in the hyperangular coordinates in the dissociation region at a large ρ = 9 bohrs. This state decays partially to the $^{16}\text{O} + ^{16}\text{O}^{18}\text{O}$ (v = 1, j = 0) channel and partially to $^{18}O + ^{16}O_2$ (v = 0, j = 16). The nodal structure along the ϕ coordinate in the lower valley ($^{18}\textrm{O}$ + $^{16}\textrm{O}_{2}\textrm{)}$ is due to the highly excited j = 16 rotational state of the ${}^{16}O_2$ dimer, while a node along the θ coordinate in the two upper valleys ($^{16}\text{O} + ^{16}\text{O}^{18}\text{O}$) is due to the vibrationally excited state of the dissociating dimer. The background picture with small triangles is the same as in Fig. 1 and helps to associate geometries of the three atoms with the amplitude of the wave function.

are around $\rho = 4$ a.u. The upper part of the figure is the view from "above" the hypersphere, along the z axis down to the xy plane, while the lower part of the figure is a view at a certain arbitrary orientation with respect to the coordinate frame. The back side of the wave function is partially hidden (the "fog" effect) to help understand relative positions of different nodal structures of the wave function. This way of representing wave functions is also used in other figures below.

III. Symmetry properties of the rovibronic wave functions

The rovibrational states of ¹⁶O¹⁸O¹⁶O and ¹⁶O¹⁶O¹⁸O are traditionally classified according to their point groups C_{2v} and C_{s} , respectively. The vibrational modes and their symmetry labels are for $^{16}O^{18}O^{16}O$ the symmetric stretch, ν_1 (A₁), the bending, ν_2 (A₁), and the antisymmetric stretch, ν_3 (B₁), modes. For $^{16}\mathrm{O}^{16}\mathrm{O}^{18}\mathrm{O}$ ν_1 denotes the $^{16}\mathrm{O}-^{16}\mathrm{O}$ stretch, ν_2 denotes the bending and ν_3 denotes the $^{16}O^{-18}O$ stretch modes, they all have symmetry A'.

Separating the ¹⁶O¹⁸O¹⁶O and ¹⁶O¹⁶O¹⁸O species is appropriate only if the energy of the molecule is near the bottom of the potential well. In our previous work,⁵⁷ we have shown that the motion of the molecule is delocalised even below the dissociation threshold, so that ¹⁶O¹⁸O¹⁶O and ¹⁶O¹⁶O¹⁸O it cannot be separated according to the classification of rovibrational states.

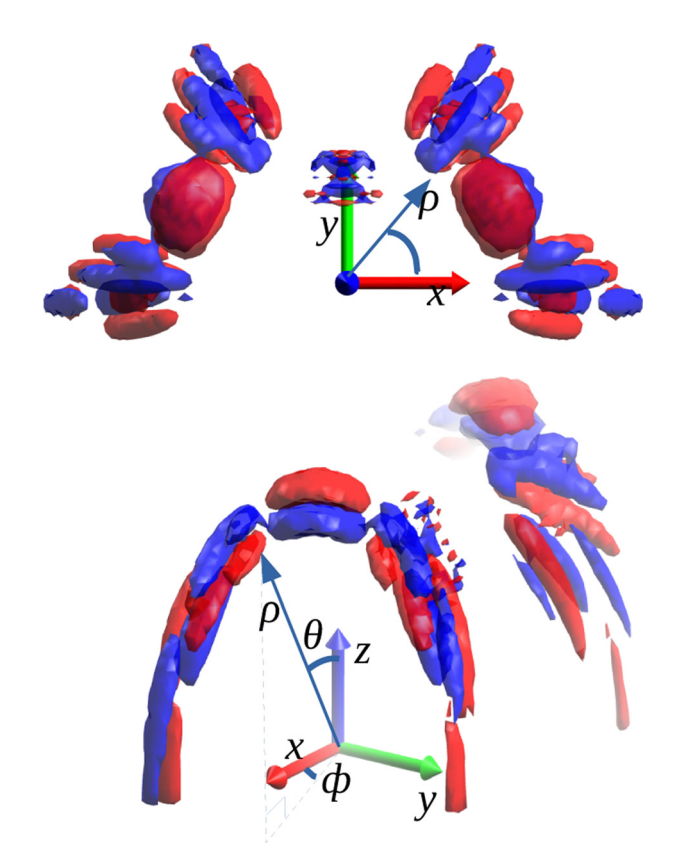


Fig. 7 Wave function (red and blue areas) of a resonant state with energy 9955 cm⁻¹ (same as in Fig. 6) shown in the three hyperangular coordinates. The lifetime of this resonance is $\tau = 210$ ps.

A more rigorous symmetry classification is obtained within the two-particle permutation inversion group, $S_2 \times I$. This group is isomorphic with the point group C_{2v} and may also be referred to as molecular symmetry group $C_{2\nu}(M)$. The irreducible representations of this group are presented in Table 1. We note here that the molecule is placed in the xz plane, which is the convention normally used in ozone spectroscopy. 122 The correspondence between the principal axes of inertia, a, b, c, and the Cartesian axes, x, y, z, is thus $(x \to b, y \to c, z \to a)$, which is the Ir representation.

The pure vibrational modes are invariant with respect to an inversion of the spatial coordinate system, the operator E^* , hence they must be either A₁ or B₁. The symmetry of the three modes $^{16}O^{16}O^{18}O$ is thus A_1 in $C_{2v}(M)$. Two equivalent forms exist of ${}^{16}O^{16}O^{18}O$: ${}^{16}O_{[1]}{}^{16}O_{[2]}{}^{18}O$ and ${}^{16}O_{[2]}{}^{16}O_{[1]}{}^{18}O$, located in the wells w₁ and w₂. Their vibrational functions will be denoted as $|\nu_1\nu_2\nu_3\rangle_1$ and $|\nu_1\nu_2\nu_3\rangle_2$, respectively. The corresponding configurations are indistinguishable and should, therefore, be symmetrized within $C_{2\nu}(M)$. Non-symmetrized wave functions are approximate and can be used only if the energy is much lower than the potential barrier between the w₁ and w₂ wells. The symmetrization yields two linear combinations:

$$|\nu_1\nu_2\nu_3; \pm\rangle_{668} = N_{\pm}(|\nu_1\nu_2\nu_3\rangle_1 \pm |\nu_1\nu_2\nu_3\rangle_2).$$
 (9)

where N_{\pm} are normalization constants. Deep in the potential wells, where tunneling can be neglected, they are $N_{\pm} = 1/\sqrt{2}$.

Table 1 Character table of the point group C_{2v} . The diatomic molecule point groups $D_{\infty\,h^{\nu}}$ and $C_{\infty\,v}$ (excerpts) and the permutation inversion group $S_2\times I$ using the nomenclatures of $C_{2v}(M)$, $D_{\infty\,h}(M)$ and $C_{\infty\,v}(M)$ for the irreducible representations

$C_{ m 2v} \ D_{ m \infty h} \ C_{ m \infty v}$			E E E	$C_{2\mathrm{b}} \ \infty {C_2}'$	$egin{array}{l} \sigma_{ab} \ \infty\sigma_{v} \ \infty\sigma_{v} \end{array}$	$\sigma_{ m bc}$ i	
$S_2 \times I$							
$C_{2v}(M)$	$D_{\infty} h(M)$	$C_{\infty}v(M)$	E	(12)	E^*	(12)*	
$\overline{A_1}$	$rac{\Sigma_{ m g}^-}{\Sigma_{ m u}^+}$	Σ^+	1	1	1	1	$p_b(p_x)$
B_1	$\Sigma_{ m u}^{+}$		1	-1	1	-1	$p_a(p_z)$
A_2	$\Sigma_{ m u}^-$	Σ^-	1	1	-1	-1	
B_2	$\Sigma_{ m g}^-$		1	-1	-1	1	$p_c(p_y)$

The two functions are symmetric ($|\nu_1\nu_2\nu_3; +\rangle_{668}$) and antisymmetric ($|\nu_1\nu_2\nu_3; -\rangle_{668}$) with respect to permutation of the two $^{16}O_2$ nuclei, operator (12), and transform as A₁ and B₁.

The vibrational functions of the $^{16}O^{18}O^{16}O$ isomer $|\nu_1\nu_2\nu_3\rangle_{686}$ are already symmetry-adapted and transform as A_1 for even values of the anti-symmetric stretch quantum number ν_3 and B_1 for odd values of ν_3 .

The rovibrational basis functions $|v_1v_2v_3JK_aK_c\rangle$ are written as

$$|\nu_1\nu_2\nu_3JK_aK_c; \pm\rangle_{668} = |\nu_1\nu_2\nu_3; \pm\rangle_{668}|JK_aK_c\rangle, \qquad (10)$$

$$|\nu_1 \nu_2 \nu_3 J K_a K_c\rangle_{686} = |\nu_1 \nu_2 \nu_3\rangle_{686} |J K_a K_c\rangle, \tag{11}$$

where $|JK_aK_c\rangle$ are asymmetric top rotational functions, and K_a and K_c are the quantum numbers for the internal projections of the total angular momentum on the a and c axes, $K_{a,c} = |k_{a,c}|$. The symmetry species of the rotational functions depend on whether the K-values are even (e) or odd (o), respectively, and are A_1 for $(K_a,K_c) = \text{ee}$, B_2 for $(K_a,K_c) = \text{eo}$, B_1 for $(K_a,K_c) = \text{eo}$, and A_2 for $(K_a,K_c) = \text{eo}$ in the present axis convention.

Not all of the rovibrational functions are physically allowed. 16 O (and also 18 O) are bosons with nuclear spin i=0, and hence only rovibrational functions of symmetry A_1 or A_2 are possible, given that the electronic wave function of the \tilde{X}^1A_1 state is totally symmetric. The symmetry classification of the rovibrational states and their spin-statistical weights are given in Table 2. We note here that tunnelling splitting cannot be observed directly, as one of the functions of the \pm -pair in eqn (10) is always symmetry forbidden due to vanishing spin weight. However, the energy difference of the two band origins may be estimated from the allowed J=1 levels under the assumption that the values of the rotational constants are the same.

Table 2 Symmetry classification of rovibrational states in $S_2 \times I$ and their statistical weights

		K_a, K_c						
Configuration	ν_3	ee	eo	oe	00			
668+	_	A ₁ (1)	B ₂ (0)	B ₁ (0)	A ₂ (1)			
668-	_	$B_1(0)$	$A_2(1)$	$A_1(1)$	$B_2(0)$			
686	Even	$A_1(1)$	$B_{2}(0)$	$B_{2}(0)$	$A_{2}(1)$			
686	Odd	$B_1(0)$	$A_2(1)$	$A_2(1)$	$B_2(0)$			

At high energies, where the three potential wells are not isolated, a distinction between $^{16}\text{O}^{18}\text{O}^{16}\text{O}$ and $^{16}\text{O}^{16}\text{O}^{18}\text{O}$ is no longer possible and their approximate spectroscopic quantum numbers do not hold anymore. The resulting states can be labelled rigorously by their symmetry, Γ , rotational quantum number, J, and the counting index n. An example of such a state delocalised between different configurations is shown in Fig. 6.

In our previous publication, ⁵⁴ we have shown that purely vibrational, *i.e.* J = 0 resonance states of ¹⁶O₃ cannot decay into O₂ + O with an outgoing l = 0 partial wave on the electronic ground state surface as such a process is symmetry-forbidden. We shall now analyse the situation for the ¹⁸O-enriched ozone, for which the three decay channels, $\kappa = 1, 2, 3$, are possible:

$${}^{16}O_{[1]}{}^{16}O_{[2]}{}^{18}O \rightarrow {}^{16}O_{[2]}{}^{18}O + {}^{16}O_{[1]}$$

$${}^{16}O_{[2]}{}^{16}O_{[1]}{}^{18}O \rightarrow {}^{16}O_{[1]}{}^{18}O + {}^{16}O_{[2]}$$

$${}^{16}O^{16}O^{18}O \rightarrow {}^{16}O_2 + {}^{18}O$$

where the first and second channels lead to identical products.

The asymptotic wave function in the exit channel κ , where κ corresponds to the index of the separating atom, can be expressed in Jacobi coordinates as¹¹⁸

$$\Psi_{\kappa \nu_{\mathbf{d}} j l}^{JM} \left(\vec{r}_{\kappa}, \vec{R}_{\kappa} \right) \approx \frac{1}{r_{\kappa} R_{\kappa}} \varphi_{\mathbf{d}}^{\mathsf{el}} \varphi_{\mathbf{d}}^{\mathsf{el}} \chi_{\nu_{\mathbf{d}} j} (r_{\kappa}) \mathcal{Y}_{j l}^{JM} (\hat{r}_{\kappa}, \hat{R}_{\kappa}) e^{i(kR_{\kappa} - l\pi/2)}, \tag{12}$$

where $\exp(i(kR_\kappa-l\pi/2))$ is the scattering function of the outgoing wave and $\chi_{v_d}(r_\kappa)$ is the rovibrational wave function of the O_2 molecule; r_κ and R_κ are the true, not mass-scaled, distances in the Jacobi coordinate system κ . M is the external projection of J. Functions $\varphi_a^{\rm el}$ and $\varphi_d^{\rm el}$ represent electronic states of the oxygen atom and the dioxygen molecule. \mathcal{Y}_{jl}^{JM} is the bipolar harmonics¹¹⁹ that couples the angular momentum, j, of the dioxygen molecule with the angular momentum, l, of the atom-diatom relative motion, to yield the total angular momentum, J. They are defined as

$$\mathcal{Y}_{jl}^{JM}(\hat{r}_{\kappa}, \hat{R}_{\kappa}) = \sum_{m_l, m_l} C_{jm_j l m_l}^{JM} Y_{j m_j}(\hat{r}_{\kappa}) Y_{l m_l}(\hat{R}_{\kappa}), \qquad (13)$$

where Y is the spherical harmonics and C is the Clebsch-Gordan coefficient.

Let us consider first the channel $^{16}O^{16}O^{18}O \rightarrow ^{16}O_2 + ^{18}O$, *i.e.* $\kappa = 3$, corresponding to the valley at the lower part of Fig. 5 with the increasing ρ . The electronic ground state of dioxygen is $X^3\Sigma_{\rm g}^-$, while that of the oxygen atom is 3P . In our paper, 54 we have examined the case $^{16}O_3$. According to Table 1, the electronic wave function of dioxygen transforms as B_2 in $C_{2\nu}(M)$. The three p-orbitals of the oxygen atom, of which two are singly occupied to form a triplet state, transform as A_1 , B_2 and B_1 , respectively, in this group, and there is a microconfiguration, $p_a^2p_bp_c$ that has $B_1^2\times A_1\times B_2=B_2$ symmetry just as the electronic wave function of the dioxygen molecule. Their product has A_1 symmetry, and hence they can dissociate on the ground state surface of ozone as far as electronic symmetry is concerned.

In fact, the product of the two electronic functions $\varphi_a^{el} \varphi_d^{el}$ in eqn (12) must always be symmetric, because within the Born-Oppenheimer approximation, the potential energy surface of the triatomic ozone, \tilde{X}^3A' , is symmetric with respect to an exchange of any two nuclei, irrespective of their isotopic masses. In the case of ¹⁶O¹⁶O¹⁸O, this may also be rationalized as follows: permutation of the two 16O nuclei rotates the molecular plane by π , and hence the perpendicular p_c atomic orbital changes its phase, as does the bipolar harmonic. The product of the electronic functions remains symmetric. The vibrational wave function of ¹⁶O₂ is symmetric, and only rotational states with odd values of j exist, such that the product $\varphi_{\rm d}^{\rm el}$ $\chi_{\nu,j}(r_{\kappa=3})$ is symmetric with respect to (12). Dissociation $^{16}\text{O}^{16}\text{O}^{18}\text{O} \rightarrow ^{16}\text{O}_2 + ^{18}\text{O} \text{ with } J = 0 \text{ implies an } l = 1 \text{ partial wave}$ of the outgoing oxygen atom.

The asymptotic functions of eqn (12) for the channels $\kappa = 1$ and 2 do not belong to a definite representation of $C_{2\nu}(M)$. The permutation operator (12) when applied to one of those functions interchanges the ¹⁶O nuclei of ¹⁶O¹⁸O the molecule and the free atom, so that

$$(12)\Psi^{JM}_{\kappa=(1,2)\nu_{\mathbf{d}}jl}(\vec{r}_{\kappa},\vec{R}_{\kappa}) = \Psi^{JM}_{\kappa=(2,1)\nu_{\mathbf{d}}jl}(\vec{r}_{\kappa},\vec{R}_{\kappa}). \tag{14}$$

The symmetric linear combination of the functions with $\kappa = 1$ and $\kappa = 2$ then transforms as A_1 in $C_{2\nu}(M)$. This result is expected as the products of the two channels are indistinguishable. There are no restrictions on the total angular momentum J, since for $^{16}O^{18}O$, both even and odd values of j are possible.

IV. Energies and lifetimes of vibrational resonances

We have computed I = 0 states above the dissociation threshold both in symmetry A₁ and B₁ up to 13 000 cm⁻¹. B₁-states are not allowed, but their I = 0 energy values represent the origins of the 668- and 686 (v_3 odd)-rovibrational bands, for which states with J > 0 do exist (see Table 2). It is then instructive to compute the corresponding band origins because they are well determined in experimental spectra analyses 102 using interpolations of a series of rotational lines to the $J \rightarrow 0$ limit. The character of these states can be understood from Fig. 8, which shows the expectation value of the hyperangle ϕ , $\langle \phi \rangle = \langle \Psi | \phi | \Psi \rangle$ as a function of energy. For both A₁ and B₁ states, the probability density is the same in the equivalent wells w_1 and w_2 , so the integral $\langle \phi \rangle = \langle \Psi | \phi | \Psi \rangle$ is evaluated only over the half of the whole interval of ϕ , in the range $-90^{\circ} \le \phi \le 90^{\circ}$ and then multiplied by two. Evaluating the integral over the whole interval $[-\pi/2;3\pi/2]$ of variation of ϕ would give an expectation value corresponding the averaged value for positions for the two equivalent wells and, therefore, would not allow to "see" where the states are primarily localized. As one can see from the figure, the states with energies below the dissociation threshold of O_2 + O, $D_0 \approx 8500 \text{ cm}^{-1}$ are localised in one of the wells, either $w_1(\phi = -30^\circ)$, equivalent to w_2 , or in $w_3(\phi = 90^\circ)$. In traditional analyses of experimental spectra¹⁰² (and references therein), these states with the expectation value around

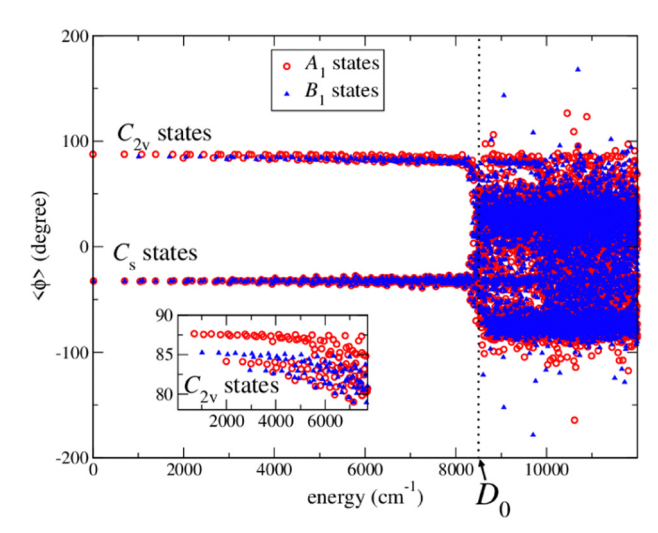


Fig. 8 Average values $\langle \Psi | \phi | \Psi \rangle$ of the hyperangle ϕ computed for the $^{50}\mathrm{O}_3$ ozone isotopologues, both for the bound and metastable states. The dissociation energy threshold $D_0 \approx 8500 \text{ cm}^{-1}$ is marked using a dotted vertical line. The states with energies below D_0 are localised in one of the wells, either in $w_1(\phi = -30^\circ)$ equivalent to w_2 , or in $w_3(\phi = 90^\circ)$. At energies near and above D_0 , the expectation value for the majority of the states is different than with $\phi = 90^{\circ}$ or -30° . These states are not localized in one of the wells.

 $\phi \approx 90^{\circ}$ are classified using the $C_{2\nu}$ point group, while the states with $\phi \approx -30^{\circ}$ are classified using the C_s point group. At energies approaching D_0 , the expectation value departs from one of the two values $\phi = 90^{\circ}$ or -30° , indicating that the highly excited bound states and the states above (vibrational continuum states) are delocalised between the three wells. We notice, however, that some states at energies above D_0 remain localised at geometries near one of the wells. These metastable states continue the series of bound vibrational resonances of highly excited bending or symmetric stretch vibrational modes, which become metastable above the dissociation limit.

The computed lifetimes of the continuum states vary by several orders of magnitude between 0.01 ps and 300 ps. The lifetimes of the A₁ states are shown in Fig. 9-11. The overall picture of lifetimes of A₁ states is shown in Fig. 9. The vertical dotted lines indicate the threshold energies for the excitation of the O_2 dimer in the dissociation channels, $v_d = 0$, 1, and 2. For each v_d , there are two thresholds close to each other and corresponding to the two different isotopologues.

The states with lifetimes around and smaller than 0.1 ps should not be considered as resonances. They are rather simple vibrational continuum states, corresponding to O + O2 halfcollisions. On the other hand, vibrational resonances having very different lifetimes, as demonstrated in Fig. 9 should have different character and different decay mechanisms.

To understand how lifetimes τ of the states are related to the type of the resonances, it is useful to consider the dependence of the lifetimes vs. energy and the averaged values $\langle \phi \rangle$, $\langle \rho \rangle$. Strictly speaking, for vibrational resonances (as well as for simple vibrational continuum states), the expectation value of the hyper-radius is undefined. However, if one limits the

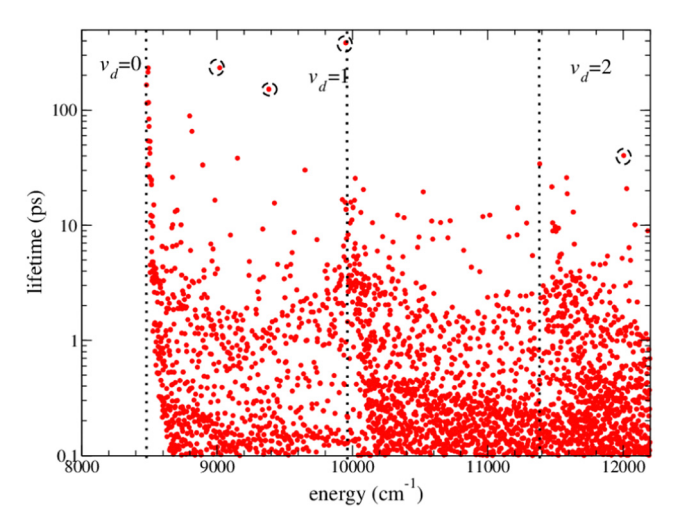


Fig. 9 Overall picture of lifetimes of A₁ states as a function of state energy. The vertical dotted lines refer approximately to the threshold energies for the excitation of the O_2 dimer $v_d = 0$, 1, and 2.

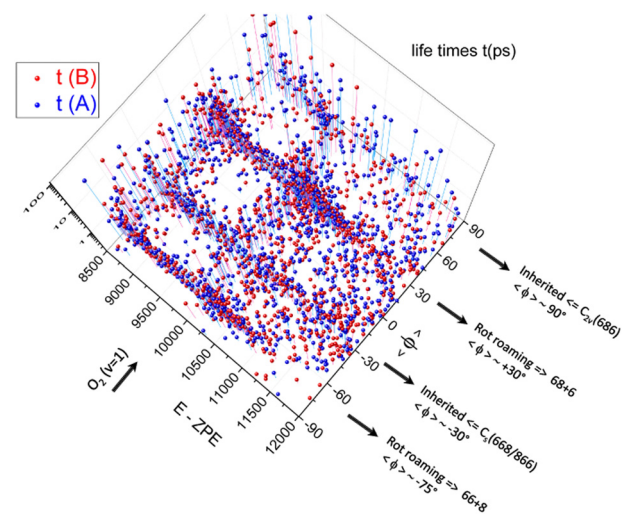


Fig. 10 Lifetimes of the vibrational resonances of the ⁵⁰O₃ isotopologues as a function of the energies E, and of the expectation value of the hyperangle $\langle \phi \rangle$. Several series clearly appear, which correspond to the physically different types of the metastable states.

interval of integration over ρ by some large, but a finite value (such as in the present numerical calculations), the expectation value $\langle \rho \rangle$ can characterize the overall size in ρ of different resonances – not absolutely – but relative to each other. At the same time, evaluating the integral $\langle \phi \rangle$ in the same way allows us to analyse the short-distance character of the states with respect to localisation in or outside of the three potential wells. Fig. 10 shows the dependence $\tau(E, \langle \phi \rangle)$ as a function of energy and $\langle \phi \rangle$ and Fig. 11 demonstrates the dependence of $\tau(E, \langle \rho \rangle)$ for the metastable states for relatively small size of the complex.

One can see from Fig. 11 that states with $\langle \rho \rangle \lesssim 4.8$ bohrs tend to have bigger lifetimes than states with larger $\langle \rho \rangle$. At such values of $\langle \rho \rangle \lesssim 4.8$ bohrs, the potential wells are still present but are already communicating, as can be seen from Fig. 2.

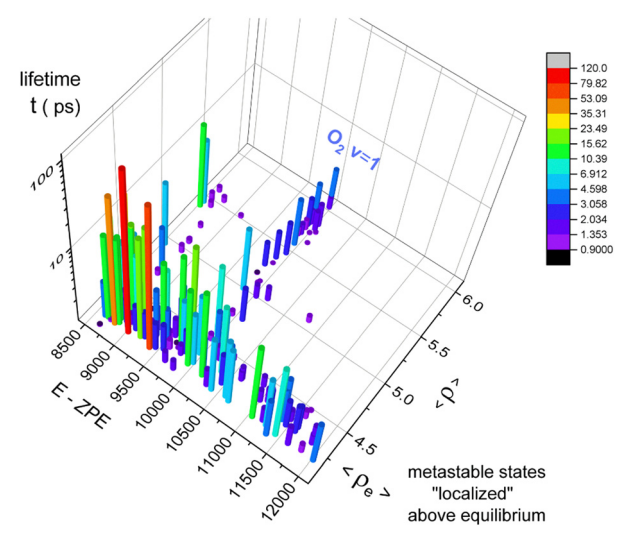


Fig. 11 Lifetimes as a function of the energies E and of the expectation value of the hyper-radius $\langle \rho \rangle$. States with $\langle \rho \rangle < 6$ a.u. are shown only.

Such resonances are metastable vibrational states of the ozone molecule. As the size of the triatomic system increases, we find states with very short lifetimes. These states are generally localized in the O_2 + O channels, which are formed at large ρ . Their character resembles more to a simple vibrational continuum state and less to a scattering resonance.

Inspecting Fig. 10, showing $\tau(E, \langle \phi \rangle)$, we notice that the largest lifetimes are found for states with low energy and $\langle \phi \rangle \approx$ 90°, which are $C_{2\nu}$ series at the potential well w₃ of the ¹⁶O¹⁸O¹⁶O isotopologue. They inherited from the metastable ¹⁶O¹⁸O¹⁶O states that have to transfer vibrational energy to the antisymmetric mode in order to decay. The states with $\langle \phi \rangle \approx$ -30° are resonances of a similar type, but sitting above the potential wells w₁ and w₂. They have lifetimes smaller than the former states, which reflects the fact that they are delocalised over the two equivalent wells. The states with $\phi \approx -75^{\circ}$ and $\phi \approx 30^{\circ}$ are the roaming states, decaying into $^{16}{\rm O_2}$ + $^{18}{\rm O}$ and ¹⁶O¹⁸O + ¹⁶O, respectively. States with relatively large lifetimes appear at the threshold energy of O_2 with ν_d = 1 vibrational excitation. The states above this threshold are in the O_2 , $v_d = 0$ continuum and are thus vibrational Feshbach resonances. They decay transferring the vibrational energy of the dimer into the kinetic energy of the O2 + O products. Typical resonances of each type are discussed below.

V. Different types of resonances: different decay mechanisms

Averaged values of ρ and ϕ give an idea about the localization of a particular vibrational resonance. Looking at the wave function of that state helps to understand to which classical motion of the three oxygen atoms the state corresponds. In this respect, there are several distinct types of resonances.

Resonances localized in the C_s potential wells

Vibrational motion of bound states at low energies is well described by the normal mode approximation in each of the w_{1,2} and w₃ wells, so that the wave function of each low-energy bound state is characterized by three quantum numbers of vibrational modes and a label whether the molecule is symmetric w_3 or not $w_{1,2}$. Vibrational levels in the same well differing by only one of the three quantum numbers form series of states with similar character of motion. At energies, approaching the dissociation limit, the normal mode approximation is, strictly speaking, not applicable. However, if the molecule stays the most of the time (in a classical description) at geometries near the minimum of the potential, the normalmode character of such states near the dissociation region is conserved. Such quantum states are present below and above the dissociative limit. They could be viewed as continuations of the corresponding low-energy normal-mode series mentioned above.

An example of such a resonance, which is mostly localized in asymmetric wells $w_{1,2}$, is shown in Fig. 12. The figure shows the wave function of the resonance by two isosurfaces, one at the value of 0.02 (two orthogonal projections xy and xz on the left) and at the value of 0.001 (similar orthogonal plots on the right). One can see that at the higher value of the isosurface, the resonance is localised in the w₁ and w₂ asymmetric wells, very similar to how bound states look like. From the upper right plot the orthogonal xy projection at the smaller amplitude value – it is evident that the wave function oscillates at large distances ρ and is present in all decay channels ¹⁶O₂ + ¹⁸O and ¹⁶O¹⁸O + ¹⁶O, therefore, indicating that the resonance decays to symmetric and asymmetric channels with comparable probabilities.

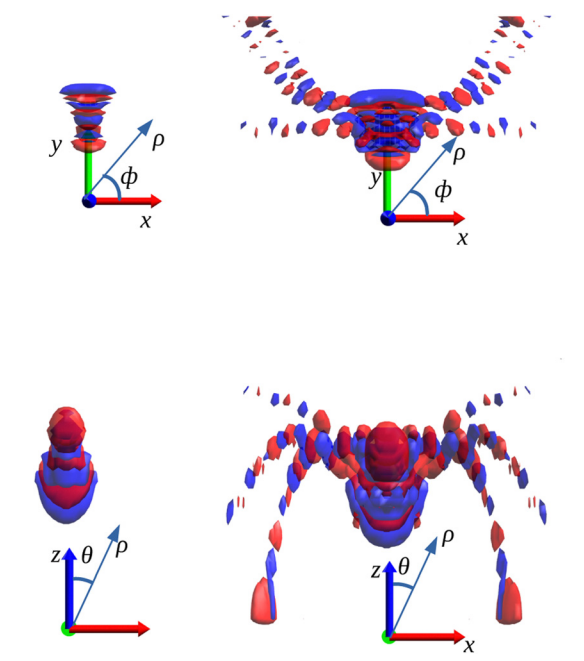


Fig. 13 The vibrational resonance with $E = 8797.59 \text{ cm}^{-1}$, $\tau = 45 \text{ ps}$, localized at small distances between O2 and O primarily at the 686 geometrical arrangement, i.e. above the w₃ well. The wave function is shown for the isosurface values of 0.02 (the two plots on the left) and 0.002 (the two plots on the right). The small-distance vibrational motion (the left plots) is a pure bending mode with 13 guanta in the mode

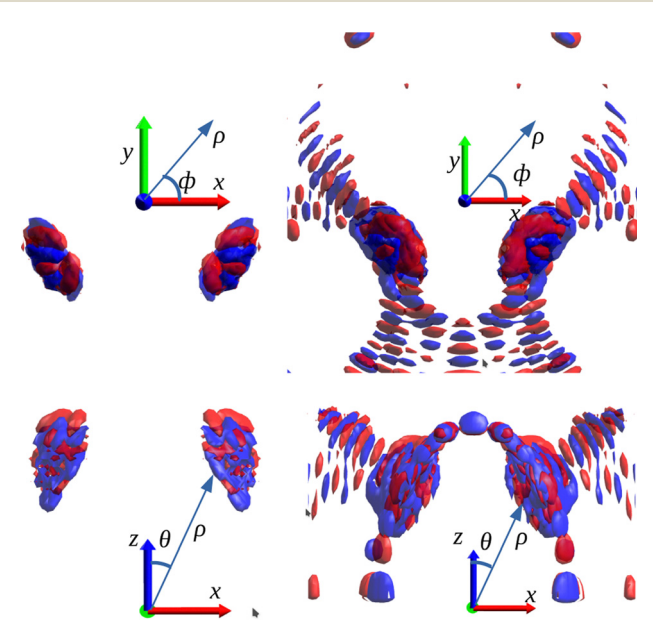


Fig. 12 The vibrational resonance with E = 8815.3 cm⁻¹, $\tau = 33$ ps, localized at small distances between $\ensuremath{\text{O}}_2$ and $\ensuremath{\text{O}},$ primarily at the 668/866 geometrical arrangements, i.e. above the w_1 and w_2 wells. The wave function is depicted for the isosurface values of 0.02 (the two plots on the left) and 0.001 (the two plots on the right).

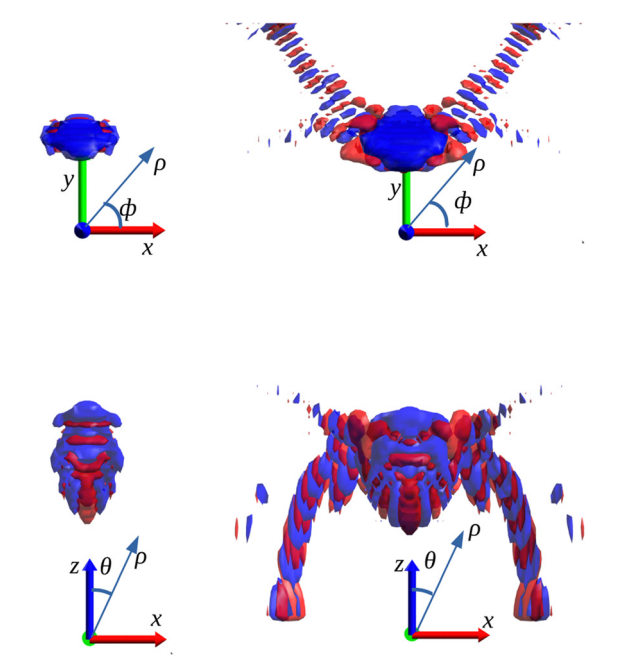


Fig. 14 Another example of a resonance – similar to the one in Fig. 13 – localized at small distances at the 686 arrangement with $E = 9385.37 \text{ cm}^{-1}$, τ = 72 ps. The isosurface values are 0.01 (the two plots on the left) and 0.001 (the two plots on the right). It is a pure symmetric-stretching-mode resonance with 9 quanta in the mode $v_{ss} = 9$.

B. Resonances localized in the $C_{2\nu}$ potential well

The second type of resonances is the continuation of series of normal-mode bound states localized in the symmetric well w₃. Wave functions of two such resonances are shown in Fig. 13 and 14. Fig. 13 shows the resonance of a pure bending mode with 13 quanta in the mode $v_b = 13$ in the symmetric well and energy 300 cm⁻¹ above the dissociative limit. The states with a smaller number of quanta v_b = 0-12 are bound. Such purebending states have the nodal structure aligned mainly along the θ coordinate near $\phi = \pi/2$. The motion along θ corresponds to the bending motion. A noticeable feature of the wave function is the dominance of the asymmetric decay channel: on the upper right plot - the xy view - the smaller-amplitude nodal structure is negligible in the ¹⁸O + ¹⁶O₂ channel. This is not surprising because it is more difficult to separate ¹⁸O than ¹⁶O in the symmetric molecule ¹⁶O¹⁸O¹⁶O.

Fig. 14 gives the wave function of the pure symmetric-stretching-mode resonance with 9 quanta in the mode v_{ss} = 9. The symmetric stretching motion corresponds approximately to the change in the hyper-radius only. Similar to the wave function in Fig. 13, the asymmetric decay channels are dominant.

The resonances localized above the potential wells have lifetimes of the order $\gtrsim 10$ ps.

C. Rotational roaming

Fig. 5 is an example of another type of resonances, specifically the rotational roaming states. Such states could be viewed as weakly-bound O_2 + O complexes where the two fragments O_2 and O rotate around each other or, looking from the molecular frame, the O2 molecule rotates with respect to the vector pointing to the O atom. The fragments stay most of the time (the largest probability) at large separations. The dissociation occurs if the energy of relative O₂ + O rotation is transferred into relative vibrational motion of the fragments, i.e. to the dissociative coordinate. Therefore, such resonances could be referred as rotational roaming resonances. They are similar in character to shape resonances in electron-atom or electronmolecule collisions, meaning that they could be viewed as if the resonant part of their wave function is bound by a centrifugal barrier due to the relative rotational motion. Another example of rotational roaming resonance is shown in Fig. 15.

The rotational roaming resonances decay relatively quickly, having lifetimes of the order of a picosecond or less. This is similar to relatively short lifetimes of shape resonances in electron-atom or electron-molecule collisions.

D. Rovibrational roaming

The rotating O_2 molecule in the rotational roaming type of resonances can also be excited vibrationally, as demonstrated by the wave function shown in Fig. 6 and 7. In this situation, the O_2 and O fragments also stay at large distances. Such resonances decay due to the energy transfer from the O_2

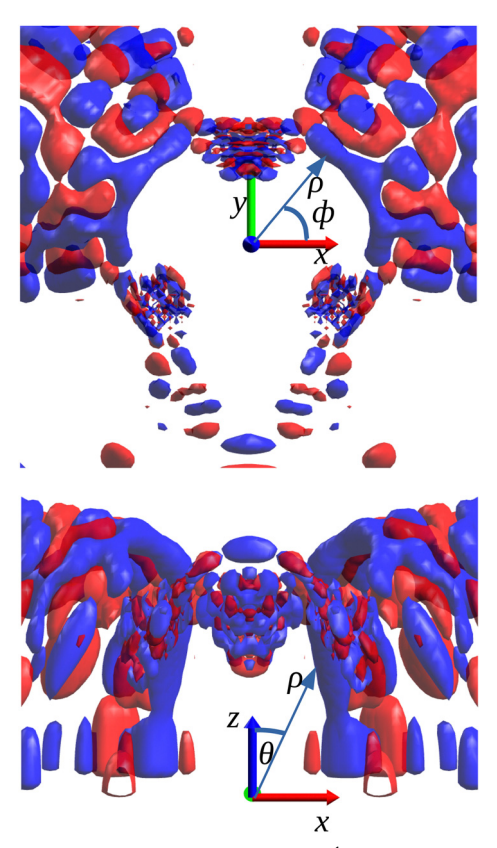
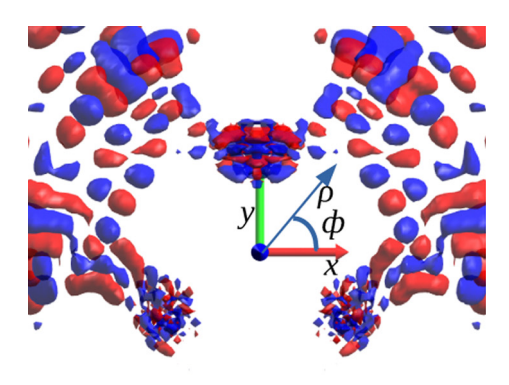


Fig. 15 The resonance with $E=8599.12~{\rm cm}^{-1}$, $\tau=3.3~{\rm ps}$, corresponding to the rotational roaming of the $^{18}{\rm O}$ oxygen around the light diatomic fragment $^{16}{\rm O}^{16}{\rm O}$. The wave function is shown for the isosurface value of 0.01. It is compared with Fig. 5, showing a similar state at a fixed value of ρ , approaching the dissociative region. Here the wave function is shown in the three dimensions, for a fixed isosurface value, showing multiple nodes in all three dimensions. The resonance is mainly localized in the valley at $\rho>6$, corresponding to the lower part of Fig. 5. This clearly indicates the decay character of the resonance.

rovibrational motion to the $\rm O_2$ + O dissociative degree of freedom. Such resonances could be referred as rovibrational roaming Feshbach resonances. They have very long lifetimes, approaching 100 ps.

E. Delocalised resonances

The largest class of resonances comprises different combinations of the above types. Fig. 16 shows an example of such a resonance. The upper panel of the figure, showing the amplitude of a larger value, demonstrates that the wave function is not negligible in the regions of the three potential wells and also in the $^{16}{\rm O}$ + $^{16}{\rm O}^{18}{\rm O}$ and $^{16}{\rm O}$ + $^{18}{\rm O}^{16}{\rm O}$ valley regions, where it has a character of the rotational roaming state, while the wave function is not visible in the $^{18}{\rm O}$ + $^{16}{\rm O}_2$ valley. The smaller amplitude figure (the lower panel) demonstrates that in the $^{18}{\rm O}$ + $^{16}{\rm O}_2$ valley, the wave function is not completely negligible and corresponds generally to rotationless motion, with no nodes along ϕ in the $^{18}{\rm O}$ + $^{16}{\rm O}_2$ dissociative channel.



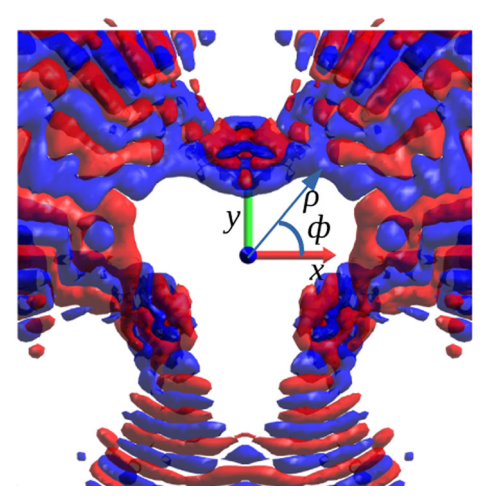


Fig. 16 An example of a resonance delocalised between the three potential wells with $E = 8757 \text{ cm}^{-1}$ and lifetime $\tau = 2.3 \text{ ps}$. The wave function is shown for isosurface values of 0.01 (upper panel) and 0.003 (lower panel).

VI. Conclusion

Energies and lifetimes of vibrational resonances were computed for the ¹⁸O-enriched isotopologue $^{50}O_3 = {^{16}O^{16}O^{18}O}$ and ¹⁶O¹⁸O¹⁶O} of the ozone molecule using hyperspherical coordinates and the method of complex absorbing potential. Various types of scattering resonances were identified, including roaming OO-O rotational states and the series corresponding to the continuation of bound vibrational resonances of highly excited bending or symmetric stretching vibrational modes. Such a series become metastable above the dissociation limit. Different paths for the formation decay of symmetric 16O18O16O and asymmetric species 16O16O18O were also identified.

Previous theoretical studies^{69,71} of the ¹⁶O¹⁶O¹⁸O system, devoted to the isotope-exchange reaction $^{16}\text{O}_2$ + $^{18}\text{O} \rightarrow ^{16}\text{O}^{18}\text{O}$ + ¹⁶O, with the same ab initio PES provided good agreement with experimental observations^{64,120} (and references therein). It was found that topographic characteristics of the full-dimensional PES shape in the neighborhood of the transition states region results in a dramatic effect in the kinetic rate constant of the reaction, which is an intermediate step in the isotopic

formation of reaction (1). Also, the recent classical trajectory calculations⁴⁰ for the formation of ozone in ternary collisions were able to reproduce several experimental observations.

Obtained energies and lifetimes of the vibrational resonances confirm the existence of many resonances in the 66 + 8 and 68 + 6 roaming channels (Fig. 10) having lifetimes of 0.3-0.5 ps, which is a typical time scale of the isotope-exchange process as was determined using the wave packet propagation method reported in ref. 71 using the same PES. On the other hand, there appear long-lived resonances with lifetimes longer by two or three orders of magnitude (Fig. 10 and 11). Such lifetimes are needed for the stabilisation process in ternary collisions.

The energies and lifetimes of the vibrational resonances computed in this work are provided in the ESI.† This information could be useful in future works to study the formation of ¹⁶O¹⁸O¹⁶O and ¹⁶O¹⁶O¹⁸O in ternary collisions, involving a diatomic oxygen, an oxygen atom, and a third particle (Ar or N₂, for example). Densities and lifetimes of resonances leading to the $^{16}\text{O}_2$ + ^{18}O dissociation channel and to the $^{16}\text{O}^{18}\text{O}$ + ^{16}O channel are different. Combined with the results of our previous calculations of resonances in the 16O3 molecule and obtained densities and lifetimes in the only one channel ¹⁶O₂ + ¹⁶O, our preliminary calculations suggest that there is a significant difference in the rate of formation of 16O3 and ¹⁶O¹⁶O¹⁸O/¹⁶O¹⁸O¹⁶O in ternary collisions.

Though the MIF issue has not yet been solved in terms of the complete theoretical first-principles modelling, the analysis of various possible types of scattering resonances and values of their lifetimes computed in this work could pave the way to further progress in the understanding of the background dynamics of this challenging problem.

Conflicts of interest

There are no conflicts to declare.

Acknowledgements

This work was supported by the Russian Science Foundation project no. 19-12-00171-P for the ozone analyses and the National Science Foundation, Grant No. 2110279 for the method of calculations. Part of this work was performed using computing resources of CRIANN (Normandy, France).

References

- 1 C. A. Brenninkmeijer, C. Janssen, J. Kaiser, T. Röckmann, T. Rhee and S. Assonov, Chem. Rev., 2003, 103, 5125-5162, DOI: 10.1021/cr020644k.
- 2 B. Luz and E. Barkan, Geochim. Cosmochim. Acta, 2005, 69, 1099-1110, DOI: 10.1016/j.gca.2004.09.001.
- 3 J. M. Eiler, Annu. Rev. Earth Planet. Sci., 2013, 41, 411-441, DOI: 10.1146/annurev-earth-042711-105348.

4 N. Dauphas and E. A. Schauble, *Annu. Rev. Earth Planet. Sci.*, 2016, 44, 709–783, DOI: 10.1146/annurev-earth-060115-012157.

- 5 M. H. Thiemens and M. Lin, *Angew. Chem.*, 2019, **131**, 6898–6916, DOI: **10.1002/ange.201812322**.
- 6 J. M. Carlstad and K. A. Boering, Annu. Rev. Phys. Chem., 2023, 74, 439–465, DOI: 10.1146/annurev-physchem-061020-053429.
- 7 N. Prantzos, O. Aubert and J. Audouze, *Astron. Astrophys.*, 1996, 309, 760–774.
- 8 C. M. Alexander and L. R. Nittler, *Astrophys. J.*, 1999, **519**, 222, DOI: **10.1086/307340**.
- M. Gounelle and A. Meibom, *Astrophys. J.*, 2007, 664, L123, DOI: 10.1086/520836.
- E. D. Young, K. Kuramoto, R. A. Marcus, H. Yurimoto and S. B. Jacobsen, *Rev. Mineral. Geochem.*, 2008, 68, 187–218, DOI: 10.2138/rmg.2008.68.9.
- 11 R. Smith, M. Gai, S. Stern, D. Schweitzer and M. Ahmed, *Nat. Commun.*, 2021, **12**, 5920, DOI: **10.1038/s41467-021-26179-x**.
- 12 T. R. Ireland, J. Avila, R. C. Greenwood, L. J. Hicks and J. C. Bridges, *Space Sci. Rev.*, 2020, 216, 25, DOI: 10.1007/ s11214-020-0645-3.
- R. N. Clayton, Annu. Rev. Earth Planet. Sci., 1993, 21, 115–149, DOI: 10.1146/annurev.ea.21.050193.000555.
- 14 E. D. Young, A. Galy and H. Nagahara, Geochim. Cosmochim. Acta, 2002, 66, 1095-1104, DOI: 10.1016/S0016-7037(01)00832-8.
- 15 H. Wiesemeyer, R. Güsten, R. Aladro, B. Klein, H.-W. Hübers, H. Richter, U. U. Graf, M. Justen, Y. Okada and J. Stutzki, *Phys. Rev. Res.*, 2023, 5, 013072, DOI: 10.1103/PhysRevResearch.5.013072.
- 16 L. Y. Yeung, J. L. Ash and E. D. Young, *Science*, 2015, 348, 431–434, DOI: 10.1007/978-3-030-33652-3_6.
- 17 P. Alexandre, *Isotopes and the natural environment*, Springer Nature, 2020, DOI: 10.1007/978-3-030-33652-3_6.
- 18 R. E. Weston Jr, Chem. Rev., 1999, 99, 2115.
- 19 M. H. Thiemens, Annu. Rev. Earth Planet. Sci., 2006, 34, 217–262, DOI: 10.1146/annurev.earth.34.031405.125026.
- 20 M. H. Thiemens, S. Chakraborty and G. Dominguez, *Annu. Rev. Phys. Chem.*, 2012, **63**, 155–177, DOI: **10.1146/annurev-physchem-**0325**11-14365**7.
- 21 M. Brinjikji and J. R. Lyons, *Rev. Mineral. Geochem.*, 2021, **86**, 197–216, DOI: **10.2138/rmg.2021.86.06**.
- 22 K. Mauersberger, *Geophys. Res. Lett.*, 1981, 8, 935–937, DOI: 10.1029/GL008i008p00935.
- 23 M. H. Thiemens and J. E. Heidenreich III, Science, 1983,
 219, 1073–1075, DOI: 10.1126/science.219.4588.1073.
- 24 J. E. Heidenreich III and M. H. Thiemens, *J. Chem. Phys.*, 1986, **84**, 2129–2136, DOI: **10.1063/1.450373**.
- 25 D. Krankowsky and K. Mauersberger, *Science*, 1996, 274, 1324–1325, DOI: 10.1126/science.274.5291.1324.
- 26 K. Mauersberger, B. Erbacher, D. Krankowsky, J. Gunther and R. Nickel, *Science*, 1999, 283, 370–372, DOI: 10.1126/ science.283.5400.370.
- 27 K. Mauersberger, D. Krankowsky, C. Janssen and R. Schinke, *Adv. At., Mol., Opt. Phys.*, 2005, **50**, 1–54, DOI: **10.1016/S1049-250X(05)80006-0**.

28 Y. Q. Gao and R. Marcus, *Science*, 2001, **293**, 259–263, DOI: 10.1126/science.1058528.

- 29 C. Janssen, J. Guenther, D. Krankowsky and K. Mauersberger, *Chem. Phys. Lett.*, 2003, **367**, 34–38, DOI: **10.1016/S0009-2614(02)01665-2**.
- 30 R. Schinke, S. Y. Grebenshchikov, M. Ivanov and P. Fleurat-Lessard, *Annu. Rev. Phys. Chem.*, 2006, 57, 625–661, DOI: 10.1146/annurev.physchem.57.032905.104542.
- 31 R. A. Marcus, *Proc. Natl. Acad. Sci. U. S. A.*, 2013, **110**, 17703–17707, DOI: **10.1073/pnas.1213080110**.
- 32 K. Feilberg, A. Wiegel and K. Boering, *Chem. Phys. Lett.*, 2013, 556, 1–8, DOI: 10.1016/j.cplett.2012.10.038.
- 33 D. Krankowsky, P. Lämmerzahl and K. Mauersberger, *Geophys. Res. Lett.*, 2000, 27, 2593–2595, DOI: 10.1029/2000GL011812.
- 34 R. Dawes, P. Lolur, J. Ma and H. Guo, *J. Chem. Phys.*, 2011, 135, 081102, DOI: 10.1063/1.3632055.
- 35 J. Guenther, B. Erbacher, D. Krankowsky and K. Mauersberger, *Chem. Phys. Lett.*, 1999, 306, 209–213, DOI: 10.1016/S0009-2614(99)00469-8.
- 36 K. Mauersberger, D. Krankowsky and C. Janssen, Solar System History from Isotopic Signatures of Volatile Elements: Volume Resulting from an ISSI Workshop 14–18 January 2002, Bern, Switzerland, 2003, pp. 265–279.
- 37 C. Janssen, PhD thesis, Ruprecht-Karls-Universität Heidelberg, 2004.
- 38 C. Janssen, *J. Geophys. Res.: Atmos.*, 2005, **110**(D8), D08308, DOI: **10.1029/2004JD005479**.
- 39 K. Luther, K. Oum and J. Troe, *Phys. Chem. Chem. Phys.*, 2005, 7, 2764–2770, DOI: 10.1039/B504178C.
- 40 M. Mirahmadi, J. Pérez-Ros, O. Egorov, V. Tyuterev and V. Kokoouline, *Phys. Rev. Lett.*, 2022, **128**, 108501, DOI: 10.1103/PhysRevLett.128.108501.
- 41 C. Janssen, J. Guenther, D. Krankowsky and K. Mauersberger, J. Chem. Phys., 1999, 111, 7179–7182, DOI: 10.1063/1.480045.
- 42 B. Hathorn and R. Marcus, *J. Chem. Phys.*, 2000, 113, 9497–9509, DOI: 10.1063/1.480267.
- 43 Y. Q. Gao and R. Marcus, *J. Chem. Phys.*, 2002, **116**, 137–154, DOI: **10.1063/1.2806189**.
- 44 Y. Q. Gao and R. Marcus, *J. Chem. Phys.*, 2007, **127**, 244316, DOI: **10.1063/1.2806189**.
- 45 C. Janssen and R. Marcus, *Science*, 2001, **294**, 951, DOI: **10.1126/science**.294.5544.951a.
- 46 R. Schinke, P. Fleurat-Lessard and S. Y. Grebenshchikov, Phys. Chem. Chem. Phys., 2003, 5, 1966–1969, DOI: 10.1039/ B301354E.
- 47 P. Reinhardt and F. Robert, *Earth Planet. Sci. Lett.*, 2013, 368, 195–203, DOI: 10.1016/j.epsl.2013.02.016.
- 48 A. Teplukhin and D. Babikov, *Faraday Discuss.*, 2018, **212**, 259–280, DOI: **10.1039/C8FD00089A**.
- 49 F. Holka, P. G. Szalay, T. Müller and V. G. Tyuterev, *J. Phys. Chem. A*, 2010, **114**, 9927–9935, DOI: **10.1021/jp104182q**.
- V. G. Tyuterev, R. V. Kochanov, S. A. Tashkun, F. Holka and P. G. Szalay, *J. Chem. Phys.*, 2013, 139, 134307, DOI: 10.1063/1.4821638.

51 R. Dawes, P. Lolur, A. Li, B. Jiang and H. Guo, J. Chem. Phys., 2013, 139, 201103, DOI: 10.1063/1.4837175.

- 52 A. Tajti, P. G. Szalay, R. Kochanov and V. G. Tyuterev, Phys. Chem. Chem. Phys., 2020, 22, 24257-24269, DOI: 10.1039/ d0cp02457k.
- 53 V. G. Tyuterev, R. V. Kochanov and S. A. Tashkun, J. Chem. Phys., 2017, 146, 064304, DOI: 10.1063/1.4973977.
- 54 D. Lapierre, A. Alijah, R. Kochanov, V. Kokoouline and V. Tyuterev, Phys. Rev. A, 2016, 94, 042514, DOI: 10.1103/ PhysRevA.94.042514.
- 55 S. Ndengué, R. Dawes, X.-G. Wang, T. Carrington Jr, Z. Sun and H. Guo, J. Chem. Phys., 2016, 144, 074302, DOI: 10.1063/1.4941559.
- 56 A. Teplukhin and D. Babikov, J. Chem. Phys., 2016, 145, 114106, DOI: 10.1063/1.4962914.
- 57 V. Kokoouline, D. Lapierre, A. Alijah and V. Tyuterev, Phys. Chem. Chem. Phys., 2020, 22, 15885-15899, DOI: 10.1039/ d0cp02177f.
- 58 A. Campargue, S. Kassi, D. Romanini, A. Barbe, M.-R. De Backer-Barilly and V. G. Tyuterev, J. Mol. Spectrosc., 2006, 240, 1-13, DOI: 10.1016/j.jms.2006.07.010.
- 59 D. Mondelain, A. Campargue, S. Kassi, A. Barbe, E. Starikova, M.-R. De Backer and V. G. Tyuterev, J. Quant. Spectrosc. Radiat. Transfer, 2013, 116, 49-66, DOI: 10.1016/ j.jqsrt.2012.10.023.
- 60 S. Vasilchenko, A. Barbe, E. Starikova, S. Kassi, D. Mondelain, A. Campargue and V. Tyuterev, Phys. Rev. A, 2020, 102, 052804, DOI: 10.1103/PhysRevA.102.052804.
- 61 S. Vasilchenko, A. Barbe, E. Starikova, S. Kassi, D. Mondelain, A. Campargue and V. Tyuterev, J. Quant. Spectrosc. Radiat. Transfer, 2022, 278, 108017, DOI: 10.1016/ j.jqsrt.2021.108017.
- 62 M. R. Wiegell, N. W. Larsen, T. Pedersen and H. Egsgaard, Int. J. Chem. Kinet., 1997, 29, 745-753, DOI: 10.1002/ (SICI)1097-4601(1997)29:10 < 745::AID-KIN3 > 3.0.CO;2-M.
- 63 M. Anderson, J. Ensher, M. Matthews, C. Wieman and E. Cornell, Science, 1995, 269, 198-201, DOI: 10.1063/1.449402.
- 64 P. Fleurat-Lessard, S. Y. Grebenshchikov, R. Siebert, R. Schinke and N. Halberstadt, J. Chem. Phys., 2003, 118, 610-621, DOI: 10.1063/1.1595091.
- 65 Y. Li, Z. Sun, B. Jiang, D. Xie, R. Dawes and H. Guo, J. Chem. Phys., 2014, 141, 081102, DOI: 10.1063/1.4894069.
- 66 Z. Sun, D. Yu, W. Xie, J. Hou, R. Dawes and H. Guo, J. Chem. Phys., 2015, 142, 174312, DOI: 10.1063/ 1.4919861.
- 67 G. Guillon, T. R. Rao, S. Mahapatra and P. Honvault, J. Phys. Chem. A, 2015, 119, 12512-12516, DOI: 10.1021/acs.jpca.
- 68 S. A. Lahankar, J. Zhang, T. K. Minton, H. Guo and G. Lendvay, J. Phys. Chem. A, 2016, 120, 5348-5359, DOI: 10.1021/acs.jpca.6b01855.
- 69 G. Guillon, P. Honvault, R. Kochanov and V. Tyuterev, J. Phys. Chem. Lett., 2018, 9, 1931–1936, DOI: 10.1021/ acs.jpclett.8b00661.
- 70 P. Honvault, G. Guillon, R. Kochanov and V. Tyuterev, J. Chem. Phys., 2018, 149, 214304, DOI: 10.1063/1.5053469.

- 71 C. H. Yuen, D. Lapierre, F. Gatti, V. Kokoouline and V. G. Tyuterev, J. Phys. Chem. A, 2019, 123, 7733-7743, DOI: 10.1021/acs.jpca.0c10395.
- 72 Z. Sun, L. Liu, S. Y. Lin, R. Schinke, H. Guo and D. H. Zhang, Proc. Natl. Acad. Sci. U. S. A., 2010, 107, 555-558, DOI: 10.1073/pnas.0911356107.
- 73 A. L. Van Wyngarden, K. A. Mar, J. Quach, A. P. Nguyen, A. A. Wiegel, S.-Y. Lin, G. Lendvay, H. Guo, J. J. Lin and Y. T. Lee, et al., J. Chem. Phys., 2014, 141, 064311, DOI: 10.1063/1.4892346.
- 74 S. A. Ndengué, R. Schinke, F. Gatti, H.-D. Meyer and R. Jost, J. Phys. Chem. A, 2012, 116, 12271-12279, DOI: 10.1021/ jp307195v.
- 75 S. Ndengué, S. Madronich, F. Gatti, H.-D. Meyer, O. Motapon and R. Jost, I. Geophys. Res.: Atmos., 2014, 119, 4286-4302, DOI: 10.1002/2013JD020033.
- 76 S. Sur, S. A. Ndengué, E. Quintas-Sánchez, C. Bop, F. Lique and R. Dawes, Phys. Chem. Chem. Phys., 2020, 22, 1869-1880, DOI: 10.1039/C9CP06501F.
- 77 P. García-Fernandez, I. B. Bersuker and J. E. Boggs, Phys. Rev. Lett., 2006, 96, 163005, DOI: 10.1103/PhysRevLett.96.163005.
- 78 A. Alijah, D. Lapierre and V. Tyuterev, Mol. Phys., 2018, 116, 2660-2670, DOI: 10.1080/00268976.2018.1473650.
- 79 R. Schinke and P. Fleurat-Lessard, J. Chem. Phys., 2005, 122, 094317, DOI: 10.1063/1.1860011.
- 80 M. V. Ivanov, S. Y. Grebenshchikov and R. Schinke, J. Chem. Phys., 2009, 130, 174311, DOI: 10.1063/1.3126247.
- 81 D. Babikov, B. Kendrick, R. Walker, R. Schinke and R. Pack, Chem. Phys. Lett., 2003, 372, 686-691, DOI: 10.1016/S0009-2614(03)00479-2.
- 82 A. Teplukhin, I. Gayday and D. Babikov, J. Chem. Phys., 2018, 149, 164302, DOI: 10.1063/1.5042590.
- 83 I. Gayday, A. Teplukhin and D. Babikov, J. Chem. Phys., 2019, **150**, 101104, DOI: **10.1063/1.5082850**.
- 84 I. Gayday, A. Teplukhin, B. K. Kendrick and D. Babikov, J. Chem. Phys., 2020, 152, 144104, DOI: 10.1063/1.5141365.
- 85 D. Babikov, E. Grushnikova, I. Gayday and A. Teplukhin, Molecules, 2021, 26, 1289, DOI: 10.3390/molecules26051289.
- 86 D. Charlo and D. C. Clary, J. Chem. Phys., 2002, 117, 1660-1672, DOI: 10.1063/1.1485069.
- 87 T. Xie and J. M. Bowman, Chem. Phys. Lett., 2005, 412, 131-134, DOI: 10.1016/j.cplett.2005.06.111.
- 88 M. Kryvohuz and R. Marcus, J. Chem. Phys., 2010, 132, 224305, DOI: 10.1063/1.3430514.
- 89 P. Reinhardt and F. Robert, Chem. Phys., 2018, 513, 287-294, DOI: 10.1016/j.chemphys.2018.07.040.
- 90 F. Robert, L. Baraut-Guinet, P. Cartigny and P. Reinhardt, Chem. Phys., 2019, 523, 191-197, DOI: 10.1016/j.chemphys. 2019.03.024.
- 91 N. Sakamoto, Y. Seto, S. Itoh, K. Kuramoto, K. Fujino, K. Nagashima, A. N. Krot and H. Yurimoto, Science, 2007, 317, 231-233, DOI: 10.1126/science.1142021.
- 92 L. Y. Yeung, L. T. Murray, A. Banerjee, X. Tie, Y. Yan, E. L. Atlas, S. M. Schauffler and K. A. Boering, J. Geophys. Res. Atmos., 2021, 126, e2021JD034770, DOI: 10.1029/ 2021JD034770.

93 S. Gromov and C. Brenninkmeijer, Atmos. Chem. Phys., 2015, 15, 1901-1912, DOI: 10.5194/acp-15-1901-2015.

- 94 B. Jonkheid, T. Röckmann, N. Glatthor, C. Janssen, G. Stiller and T. Von Clarmann, Atmos. Meas. Tech., 2016, 9, 6069-6079, DOI: 10.5194/amt-9-6069-2016.
- 95 C.-H. Huang, S. Bhattacharya, Z.-M. Hsieh, Y.-J. Chen, T.-S. Yih and M.-C. Liang, Earth Space Sci., 2019, 6, 752-773, DOI: 10.1029/2018EA000517.
- 96 L. Y. Yeung, L. T. Murray, P. Martinerie, E. Witrant, H. Hu, A. Banerjee, A. Orsi and J. Chappellaz, Nature, 2019, 570, 224-227, DOI: 10.1038/s41586-019-1277-1.
- 97 M. Evans, Nature, 2019, 570, 167-168, DOI: 10.1038/ d41586-019-01752-z.
- 98 C. Janssen and B. Tuzson, J. Phys. Chem. A, 2010, 114, 9709-9719, DOI: 10.1021/jp1017899.
- 99 F. Robert and P. Reinhardt, Chem. Phys. Impact, 2022, 4, 100073, DOI: 10.1016/j.chphi.2022.100073.
- 100 M. Sierra-Olea, S. Kölle, E. Bein, T. Reemtsma, O. J. Lechtenfeld and U. Hübner, Water Res., 2023, 233, 119740, DOI: 10.1016/j.watres.2023.119740.
- 101 V. G. Tyuterev, R. Kochanov, A. Campargue, S. Kassi, D. Mondelain, A. Barbe, E. Starikova, M. R. De Backer, P. G. Szalay and S. Tashkun, Phys. Rev. Lett., 2014, 113, 143002, DOI: 10.1103/PhysRevLett.113.143002.
- 102 A. Barbe, S. Mikhailenko, E. Starikova and V. Tyuterev, Molecules, 2022, 27, 911, DOI: 10.3390/molecules27030911.
- 103 D. J. Tannor, J. Am. Chem. Soc., 1989, 111, 2772-2776.
- 104 B. R. Johnson, J. Chem. Phys., 1983, 79, 1916, DOI: 10.1063/ 1.445970.
- 105 V. Kokoouline and F. Masnou-Seeuws, Phys. Rev. A: At., Mol., Opt. Phys., 2006, 73, 012702, DOI: 10.1103/PhysRevA.73.012702.
- 106 J. Blandon, V. Kokoouline and F. Masnou-Seeuws, Phys. Rev. A: At., Mol., Opt. Phys., 2007, 75, 042508, DOI: 10.1103/ PhysRevA.75.042508.
- 107 J. Blandon and V. Kokoouline, Phys. Rev. Lett., 2009, 102, 143002, DOI: 10.1103/PhysRevLett.102.143002.

- 108 A. Alijah, J. Mol. Spectrosc., 2010, 264, 111-119, DOI: 10.1016/j.jms.2010.09.009.
- 109 A. Alijah and V. Kokoouline, Chem. Phys., 2015, 460, 43, DOI: 10.1016/j.chemphys.2015.04.020.
- 110 D. Townsend, S. A. Lahankar, S. K. Lee, S. D. Chambreau, A. G. Suits, X. Zhang, J. Rheinecker, L. Harding and J. M. Bowman, Science, 2004, 306, 1158-1161, DOI: 10.1126/ science.1104386.
- 111 A. G. Suits, Acc. Chem. Res., 2008, 41, 873-881, DOI: 10.1021/ar8000734.
- 112 J. M. Bowman, Mol. Phys., 2014, 112, 2516-2528, DOI: 10.1080/00268976.2014.897395.
- 113 F. A. Mauguière, P. Collins, Z. C. Kramer, B. K. Carpenter, G. S. Ezra, S. C. Farantos and S. Wiggins, J. Chem. Phys., 2016, 144, 054107, DOI: 10.1063/1.4940798.
- 114 R. C. Whitten and F. T. Smith, J. Math. Phys., 1968, 9, 1103, DOI: 10.1063/1.1664683.
- 115 O. I. Tolstikhin, S. Watanabe and M. Matsuzawa, J. Phys. B: At., Mol. Opt. Phys., 1996, 29, L389, DOI: 10.1088/0953-4075/29/11/001.
- 116 I. Tuvi and Y. B. Band, J. Chem. Phys., 1997, 107, 9079-9084, DOI: 10.1063/1.475198.
- 117 V. Kokoouline, O. Dulieu, R. Kosloff and F. Masnou-Seeuws, J. Chem. Phys., 1999, 110, 9865, DOI: 10.1063/ 1.478860.
- 118 N. Douguet, J. Blandon and V. Kokoouline, J. Phys. B: At., Mol. Opt. Phys., 2008, 41, 045202, DOI: 10.1088/0953-4075/ 41/4/045202.
- 119 A. M. Arthurs and A. Dalgarno, Proc. R. Soc. London, Ser. A, 1960, 256, 540-551, DOI: 10.1098/rspa.1960.0125.
- 120 S. Anderson, D. Hülsebusch and K. Mauersberger, J. Chem. Phys., 1997, 107, 5385-5392, DOI: 10.1063/1.474247.
- 121 P. R. Bunker and P. Jensen, Molecular Symmetry and Spectroscopy, NRC Research Press, 1998.
- 122 This choice is different from that of Bunker & Jensen. 121 As a result, the symmetry labels B₁ and B₂ are interchanged.